Characterisation of structured and functionalised particles by small-angle X-ray scattering (SAXS)

Hermann Nirschl, Xiaoai Guo*

Insitute for Mechanical Process Engineering and Mechanics, Karlsruhe Institute of Technology, Strasse am Forum 8, 76131 Karlsruhe, Germany

Keywords:
Small-angle X-ray scattering (SAXS)
Functionalised particles
Nanostructured materials
Particle size analysis
Crystalline structure
Morphology

A B S T R A C T

In this work we provided an overview about the use of small-angle X-ray scattering (SAXS) technology for non-invasive characterisation of nanostructured and functionalised particles. Firstly, we demonstrated our modular-designed laboratory SAXS camera with different options and possibilities for quick *in-situ* measuring various disperse particulate systems including powders and suspensions as well as aerosol nanoparticles which can be deposited on a certain substrate. The detection angle reaches 90°, allowing simultaneous wide-angle X-ray scattering (WAXS) measurement on the crystalline structures. Further extension of the sample-to-detector distance enables multi-level structural characterisation of particle systems ranging from about one nanometer to several hundred nanometers. The use of an on-line X-ray detector makes on-line *in-situ* analysis possible. Secondly, different data processing methods and models have been introduced for analyzing the acquired scattering data and retrieving the structural parameters of the investigated particle systems. Finally, we presented some selected experimental results obtained by SAXS–WAXS, including commercial nanoparticles, and laboratory-synthesized nanostructured and functionalised particles such as silica multiplets, silica-magnetite core–shell nanocomposites, metallic nanoparticles and catalyst nanodots on oxide support particles in different liquid- and gas-phase synthesis processes as well as nanostructured particles in particle handling processes like high pressure dispersion and high temperature calcination.

1. Introduction

Nanostructured and functionalised particles possess unique properties (*e.g.* optical, chemical, physical, electrical, *etc.*) and find many applications due to their sizes, morphologies and structures. Knowledge of their structural parameters helps to improve the performace and control product quality during synthesis and/or in post-handling processes. These particle systems can be studied with different techniques like imaging, scattering, centrifugal, gas adsorption, spectroscopy, and so on. Among them, small-angle X-ray scattering (SAXS) is a non-invasive technique and has proven to be a very powerful tool for structural characterisation of particle systems under their native or realistic conditions (Guinier and Fournet, 1955). Basically, two scattering modes, transmission and reflection (grazing incidence), are used for SAXS measurements. Grazing incidence mode, generally called GISAXS, is often used for characterisation of nanostructured films and surfaces (Renaud et al., 2009). In this work we focus on the transmission SAXS by placing the sample normal to the incident beam. The samples to be analysed can be dry powders, particle suspensions, aerosol particles, which are sometimes deposited on a certain substrate, or other two-phase disperse systems. SAXS measures the excess electron density, i.*e.* the density difference between particles and their surrounding medium, thus porous structures can also be probed just by considering a pore as an "inverse" particle. This implies that SAXS can also probe the closed pores which are not accessible to gas adsorption (BET) instrument. The scattering intensity is measured as a function of the scattering angle 2θ. To better understand the interaction of the X-ray with materials, a brief physical background of SAXS will be given in Section 2. In general, SAXS detector records elastic scattering of X-rays at angles close to the direction of incident beam, say, $2\theta < 5°$. This

* *Corresponding author*.
E-mail address: hermann.nirschl@kit.edu (H. Nirschl).

limit depends on the SAXS setup. SAXS experiments give information on objects in the size range between 1 and 100 nm. However, use of the Bonse–Hart configuration (Bonse and Hart, 1965) or a very long sample-to-detector distance can achieve ultrasmall-angle X-ray scattering (USAXS), which is capable of probing structures in the size range of 1–1000 nm. SAXS data contain the information on primary particle and agglomerate size, their size distribution, structure, specific surface area and functionalisation like coating layer thickness or the structure of nanocomposites.

This article wants to give an overview concerning the possibilities of using the SAXS technology for particle characterisation on the nanometer scale. Starting from the physical background, detailed information is given about the development of modular-designed SAXS laboratory cameras. Although the high intensity of the X-rays in a synchrotron facility is preferable for X-ray scattering measurements, especially for characterizing weaker scatters, laboratory cameras have their advantages considering the permanent availability and unlimited design options. The main physical relations for analysis of scattering curves with different methods and models are presented starting from single spheres via aggregates to the analysis of mulitplets and size distributions. Furtheron the X-ray scattering methods have been extended for the description of nanoscale coatings, nanodots on nanospheres and nanocomposites as well as for investigations on crystalline structures and crystal phase transformation at wide angles.

2. Physical background of SAXS

The basis process of the scattering of X-rays by materials is the photon-electron interaction. In the SAXS experiments performed in transmission mode, the maximum scattering intensity is related to the sample thickness which is approximately inverse proportional to the linear absorption coefficient (Sakka, 2005). For long wavelength ($\lambda \gg 0.1$ nm), a very thin sample should be used due to very high absorption, whereas for very short wavelength ($\lambda \ll 0.1$ nm), the scattering concentrated at extremely small angles will make practical analysis very difficult. Therefore, SAXS usually utilizes monochromatic X-rays with wave lengths in the range of *ca.* 0.05–0.25 nm. Detailed information about the SAXS theory is provided in some classical SAXS books (Guinier and Fournet, 1955; Glatter and Kratky, 1982). Here we will not go into detail but intend to give a very brief description of the physical background of SAXS, which will help readers to better understand the analysis and interpretation of SAXS experimental data later.

The interaction of X-rays with electrons of matter leads to different processes such as refraction, diffraction, absorption and scattering. The refractive index of all materials is close to 1 for X-rays and thus the refraction can be neglected. In the transmission SAXS mode, the transmitted beam will be attenuated through inelastic scattering, fluorescence and thermal effect, depending on the material density and composition. Absorption can be corrected in the SAXS experiment. The diffraction can be neglected. Low diffraction of X-rays and the geometry of the measurement set-up, where the sample-to-detector distance is much larger than the particle size, which itself is much larger than the wavelength, allow for simplification of the analysis by the Fraunhofer approximation (Guinier and Fournet, 1955; Wengeler, 2007). Thus, scattering occurs solely at the electrons of the material investigated. These electrons are accelerated by X-rays and emit secondary spherical waves with identical frequency (or wave length λ) but different phases. The scattered X-rays of a large number of scattering centres superimpose to the scattering intensity.

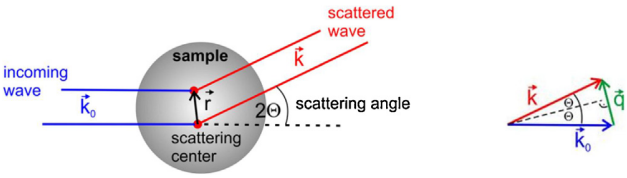

Fig. 1 – Scattering geometry represents the incoming X-rays with the wave number vector $\vec{k}_0$ and the scattered X-rays with the wave number vector $\vec{k}$ at a scattering angle 2θ. The difference between both wave vectors is described by the scattering vector $\vec{q}$.

Fig. 1 shows the scattering geometry. Incident X-rays are characterized by the wave number vector $\vec{k}_0$ with a modulus of $2\pi/\lambda$ and the secondary waves are described by the wave number vector $\vec{k}$. Their difference results in a scattering vector of $\vec{q} = \vec{k} - \vec{k}_0 = 4\pi/\lambda \cdot \sin\theta$ for small angles. The scattering amplitude results from the superposition of waves scattered from all single scattering centres considering the phase difference $\vec{q} \cdot \vec{r} = \left(\vec{k} - \vec{k}_0\right) \cdot \vec{r}$. Thus, the total intensity stems from the integration of scattering intensities of all electrons in a scattering volume. Because of the large number of electrons in scattering objects even on the nanoscale a continuous description is commonly used. The scattering amplitude $A\left(\vec{q}\right)$ can mathematically given by the Fourier transform of the electron density distribution $\rho_e\left(\vec{r}\right)$ in the real space

$$A\left(\vec{q}\right) = A_e \int_V \rho_e\left(\vec{r}\right) e^{-i\vec{q}\cdot\vec{r}}\, d\vec{r} \tag{1}$$

with A_e as the amplitude of a single electron. The Fourier transform allows in the transformed space the analysis of periodic structures of the electron density in the real space due to phase differences. For example, regularly ordered particles in a homogeneous media are such structures. The resulting scattering intensity is given by the square of absolute values of the scattering amplitude $I\left(\vec{q}\right) = |A\left(\vec{q}\right)|^2$. Therefore amplitudes of all scattering centres $\vec{r}_i$ and all possible distances to the scattering centre $\vec{r}_i - \vec{r}$ are integrated. This corresponds to the Fourier transform of the autocorrelation function of the electron density

$$I\left(\vec{q}\right) = I_e \int_V \tilde{\rho}_e^2\left(\vec{r}\right) e^{-i\vec{q}\cdot\vec{r}}\, d\vec{r} \tag{2}$$

where I_e is the scattering intensity of one single electron.

The vectorial autocorrelation function $\tilde{\rho}_e^2$ is the Patterson function:

$$\tilde{\rho}_e^2\left(\vec{r}\right) = \int_V \rho\left(\vec{r}_i\right) \rho\left(\vec{r}_i - \vec{r}\right) d\vec{r}_i \tag{3}$$

This equation can be simplified by introducing the excess electron density $\Delta\rho_e\left(\vec{r}\right)$ as the difference between electron density of the particles and the surrounding matrix. For isotropic systems the expression $\langle e^{-i\vec{q}\cdot\vec{r}} \rangle = \sin(qr)/(qr)$ can be averaged in all spatial directions (Glatter and Kratky, 1982). The Patterson function can also be averaged in space, which results in an angular averaged autocorrelation function

$\gamma(r) = \langle \tilde{\rho}_e^2 \left(\vec{r} \right) \rangle$ and the scattering intensity $I(q)$ is normalized by I_e

$$I(q) = 4\pi \int_0^\infty \gamma_0(r) \frac{\sin qr}{qr} r^2 dr \quad (4)$$

where the characteristic function $\gamma_0(r) = \gamma(r)/\gamma(0)$ describes the spatial distribution of particles. It is interpreted as probability that a point in a distance r from any other point in space is inside a particle. Thus for scattering of a single particle it is monotonously decreasing, positive and takes the value 0 for $r > d_{max}$, with a maximum particle extension of d_{max}. In SAXS measurements, usually different models are used to analyse experimental scattering curves and retrieve the information on the structures and sizes. Details on the data processing and interpretation will be given and further discussed in following sections by means of some selected application examples.

3. Experimental

3.1. *Development of laboratory SAXS camera systems*

Since the first so-called Kratky SAXS camera was developed in the 1950s (Kratky, 1954), it has become one of the most widely used laboratory equipments for structural analysis (Glatter and Kratky, 1982). Its main components are the X-ray tube, the X-ray collimation and the detector. For characterisation of large structures of particles the original SAXS camera has been optimized and extended with different features (Dingenouts and Ballauff, 1998). Fig. 2 shows some labroratory SAXS camera systems which have been designed and further developed to meet different requirements on structural characterisation at our laboratory in recent years. A fine focus X-ray tube equipped with a copper cathode (Cu–K_α radiation, $\lambda = 0.154$ nm) is selected for measurements. The X-rays are collimated by a block collimation system, which allows the resolution of very small angles. Compared to point collimation, the block collimation almost completely suppresses parasitic scattering for small angles and leads to a higher intensity of the X-ray beam. Despite of the block collimation the measurement time of the equipment for *in-situ* characterisation was much too long (several hours), depending on the count rate of detector and the electron density contrast of particle systems. To focus the diverging beam and to increase the intensity even more, a specific X-ray optic, called Göbel mirror (AXO, Dresden GmbH, Germany) was installed between X-ray tube and the collimation system, as schematically illustrated in Fig. 2a. The camera was originally equipped with a one-dimensional position sensitive gas-filled detector (PSD 50m, MBraun) which has a resolution of 25.4 μm at 2048 channels and a dynamic range of about four decades (Fig. 2b). The elliptic curved Goebel mirror transforms the divergent, polychromatic X-ray to a monochromatic, focussed primary beam with a defined wave length. Furthermore, a beam stop was designed and installed in front of the detector so that the primary beam is partly absorbed for determination of the zero point of the scattering vector ($q = 0$).

The gas-filled detector has been replaced with a two-dimensional imaging plate detector to improve the detection of the scattered signal (Fig. 2c). According to preliminary suggestions (Fritz and Bergmann, 2006), these devices lead to a significant reduction of measurement time, an improvement on spatial resolution regarding the scattering vector and an increase of the dynamic range. Later on, the SAXS camera configuration has been further developed by extending the measuring range of scattering angle 2θ. Imaging plate can be arranged in a curved manner so that the configuration is able to determine the intensity at small and large scattering angles up to 90°, as shown in Fig. 2d. This allows simultaneous measurement of the SAXS signal with a wide-angle X-ray scattering (WAXS) detection (Guo et al., 2015a,b). So, besides the determination of agglomerate and particle structure, crystallinity or even the chemical compostion of the sample can be determined. The disadvantage of the imaging plate is the offline data acquistion *via* an external laser scanner (Fujifilm FLA-7000). In case of measuring reacting particle systems on a short time scale, the imaging plate can be replaced with an online X-ray detector (Dectris Pilatus 100K, Switzerland), which operates in "single photon counting" mode based on advanced CMOS technology with no dark current or readout noise but a high dynamic range. Dynamic *in-situ* experiments are possible when the sample chamber is designed for a flow configuration. This modular design allows continuous passage of the reactants through a sample cell inside the measurement chamber and thus direct observation of the particle formation process.

Above laboratory SAXS–WAXS camera system allows characterisation of nano-structured materials and functionalised nanoparticles with a size of up to approximately 80 nm as well as their crystalline structures. By further increasing the sample-to-detector distance from 230 mm up to 1300 mm by means of a new Göbel mirror with long focus lengths, as depicted in Fig. 2e, the minimum scattering vector q can be decreased by a factor of 10 down to a value of 0.008 nm^{-1} corresponding to a structure size of up to 780 nm. The modified ultrasmall- and wide-angle X-ray scattering (USAXS–WAXS) laboratory setup enables structural analysis of particle systems on multiple scales ranging from about one nanometer to several hundred nanometers (Gutsche et al., 2017). Nevertheless, the intensity of usual laboratory X-ray sources is limited so that a synchrotron radiation facility with a higher X-ray flux, *e.g.* ESRF in Grenoble, is the best alternative for even further extension of detectable size to larger structures and reduction of measurement time. The availability of synchrotron X-ray sources is limited, whereas the laboratory equipment is usually available with no restriction. Those recently developed and further optimized laboratory measuring systems are very suitable for investigation of different nanostructured materials and functionalised nanoparticle systems in the fields of chemical reaction, process engineering, particle synthesis and post-handling as well as material science.

3.2. *SAXS measurements*

SAXS measurements can be performed by using an easily accessible laboratory camera system and/or a synchrotron beamline. To achieve high scattering intensity, a 2D area detector is usually used to detect the angle-resolved signals which are elastically scattered by the investigated samples. To provide an overview of the possibilties of using laboratory SAXS instruments for particle characterisation on the nanometer scale, some selected nanostructured materials and functionalised nanoparticles have been investigated by means of our recently developed and further optimized laboratory camera systems, as depicted in Fig. 2. For the characterisation of suspensions, particle systems were dispersed in a solvent and stabilized, and then filled into a thin-walled quartz capillary

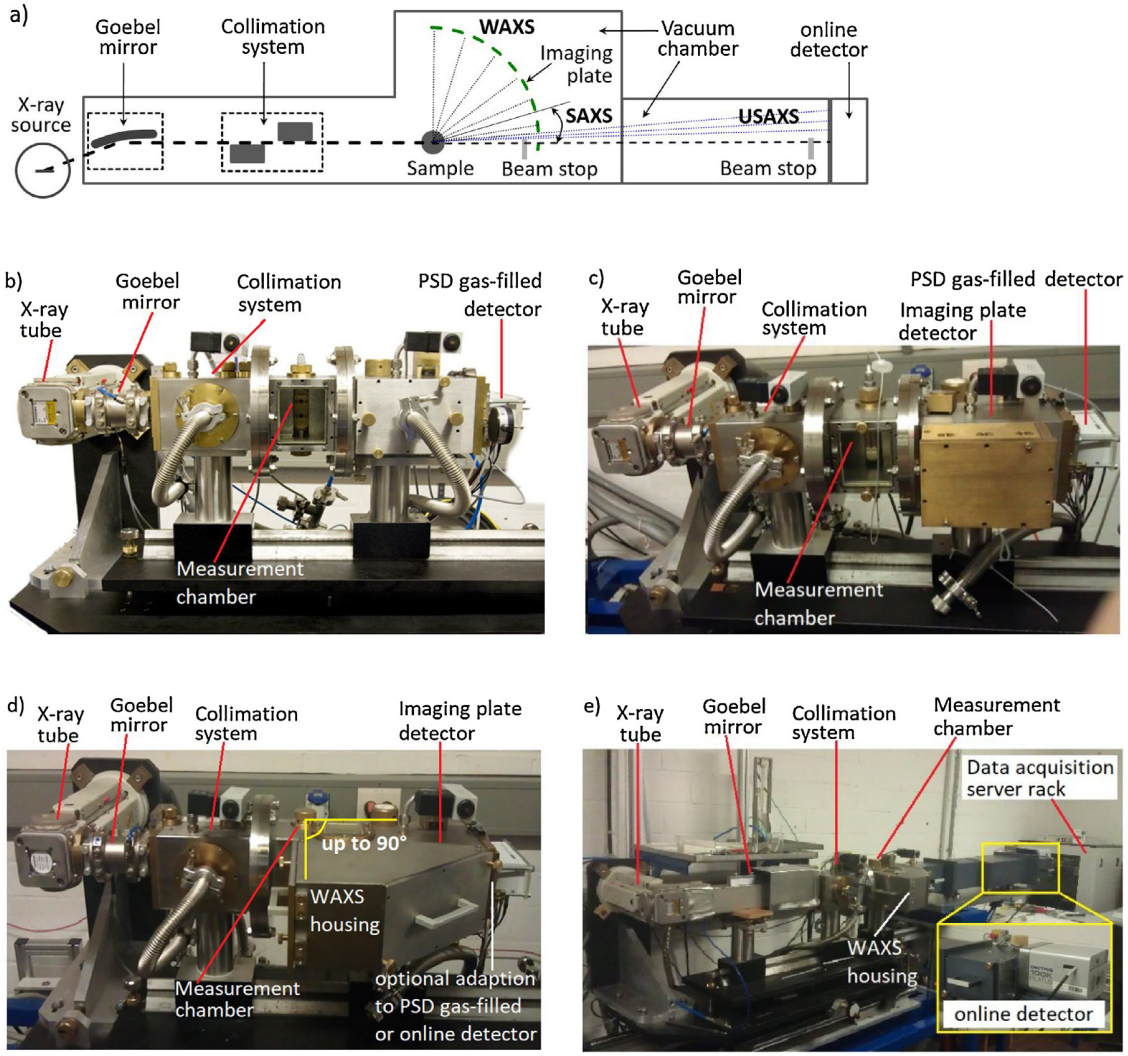

Fig. 2 – Development of laboratory X-ray scattering camera systems for characterisation of nanostructured materials and functionalised particles. (a) Schematic ray tracing of modified Kratky camera with Goebel mirror and collimation system together with an optional USAXS modul. (b) SAXS camera with a PSD gas-filled detector; (c) SAXS camera with a PSD gas-filled detector and an alternative imaging plate detector; (d) SAXS–WAXS camera with a curved imaging plate detector for simultaneous measurements at scattering angles 2θ up to 90° with an alternative adaption to a PSD gas-filled detector and an online Dectris Pilatus detector; (e) USAXS–WAXS camera equipped with an online Dectris Pilatus detector.

with an internal diameter of 1 mm using a syringe. For the measurements of powders or aerosols, the samples under study were first carefully distributed or deposited onto a sample substrate, such as an adhesive tape (tesa SE), and then positioned in a specially designed sample holder inside the measurement chamber. Besides, corresponding particle-free solvent and sample substrate were also measured under the same conditions so as to realize the background subtraction later. For dynamic *in-situ* experiments, syringe pumps were used for continuous passage of the reactants through the sample cell inside the measurement chamber, allowing direct observation of the particle formation process.

In some cases, the absolute scattering intensity is necessary for determination of particle number concentration and mean molecular weight. Calibration of absolute instensity can be done using standard calibrating materials such as, water, pure liquids, monodisperse colloidal suspensions and glassy carbon (Orthaber et al., 2000; Dreiss et al., 2006; Fan et al., 2010; Zhang et al., 2010; Gutsche et al., 2016). The use of absolute instensity has advantages like independence of measurement time, sample thickness and camera geometry. The absolute instensity is not necessary for determination of the correlation function and structural parameters, *i.e.* in this case the measured scattering intensity is often reported in arbitrary units. In the SAXS experiments, the background signal originating from the sample cell or support substrate and optics itself should be taken into consideration. Usually the background effect can be removed by subtracting the scattering intensity of the used empty sample cell or support substrate. The scattering intensity from particles in a dilute suspension can be corrected by subtracting the scattering of solvent in cell from that of particle suspension in cell. Consequently, the obtained scattering curves are analysed with different approaches and models to retrieve the information on the structures and sizes of the studied particle systems, which are given below, respectively.

To observe the surface property and particle size, a transmission electron microscope (TEM, Philips CM12, operating at 120 kV) was used to characterize the samples which were prepared by dipping the carbon-coated TEM grids into the diluted dispersions and drying in air. In addition, other measurement techniques such as analytical ultracentrifuge (AUC, Beckman

Coulter Optima XLI) and nitrogen adsorption (BET, Autosorb-1, Quantachrome instruments) have also been utilized for particle size analysis and characterisation of specific surface area, respectively.

3.3. *Data processing*

The resulting scattering curves are analysed with differential and integral parameters for the appoximation of the characteristic function (Guinier and Fournet, 1955; Glatter and Kratky, 1982; Feigin and Svergun, 2013). The radius of gyration R_G is an important integral parameter, defined as follows

$$R_G^2 = \frac{\int_0^\infty \gamma_0(r) r^4 dr}{2 \cdot \int_0^\infty \gamma_0(r) r^2 dr} \tag{5}$$

which is equivalent to the mass specific radius of gyration of classical mechanics. R_G can be considered as the electronic radius of gyration of the particle about its electronic centre of mass. The geometric diameter d_p can be determined by $d_p = 2\sqrt{5/3}R_G$. The relationship between the scattering intensity $I_0(q)$ of a single particle at low q and the radius of gyration R_G can be described with Guinier law (Guinier and Fournet, 1955)

$$I_0(q) \approx I_0(0) \cdot e^{-\frac{q^2 R_G^2}{3}} \tag{6}$$

It results from a series of potentials applying a Taylor series expansion (Glatter and Kratky, 1982). Additionally, the scattering intensity at high q is characterised by the Porod constant C_p, which is defined for systems with interfaces between phases with a discrete jump in the electron density. The Porod constant C_p is determined by the surface of the particle S_p and the excess electron density $\Delta\rho_e$.

$$C_p = \lim_{q\to\infty} I(q) \cdot q^4 = 2\pi\Delta\rho_e^2 S_p. \tag{7}$$

From this relation the mass-related specific surface area (*SSA*) for a single particle or an aggregated configuration can be calculated

$$SSA = \frac{S_p}{\rho_p \cdot V_p} = \frac{\pi}{\rho_p}\frac{C_p}{Q}, \tag{8}$$

where ρ_p is the particle density and Q is the so-called scattering invariant

$$Q = \int_0^\infty q^2 I(q) dq = 2\pi^2 \Delta\rho_e^2 V_p, \tag{9}$$

accounting for the total particle volume V_p.

Single particle scattering is described by the form factor $P(q) = I_0(q)/I_0(0)$. For the special case of a spherical particle with a radius R and uniform denisty, the form factor can be given by

$$P(q) = \left[3\frac{\sin(qR) - qR\,\mathrm{co}\,(qR)}{q^3 R^3}\right]^2 \tag{10}$$

The interference is included by a structure factor $S(q)$. The scattering of a multi-particle system results from the single particle scattering and the interference of the single particle scattering patterns

$$I(q) = \frac{N}{V}\Delta\rho_e^2 V_p^2 P(q) S(q) \tag{11}$$

with N/V as the particle number concentration.

$P(q)$ and $S(q)$ consist of an integral part, which is determined by constructive interference of the scattered X-rays, and a structural part of scattering, where accidential interference occurs (Sorensen, 2001). The integral part, called Guinier range, is given by Guinier law and is limited by $qR_G < 1$. The structural part is characterized by power-law behaviour of the scattering function $I(q) \sim q^{-P}$ for $qR_G > 1$. In this way, the particle size and specific surface area can be dertermined.

The structure factor $S(q)$ results from the interference of the scattering pattern of the primary particles. For agglomerate with known primary particle sizes and positions the total scattering intensity $I(q)$ is calculated as (Debye, 1915; Guinier and Fournet, 1955)

$$I(q) = \sum_i I_{0,i}(q) + 2 \cdot \sum_{i=1}^{n-1}\sum_{k=i+1}^{n} A_k(q) A_i(q) \cdot \frac{\sin(q r_{ki})}{q r_{ki}} \tag{12}$$

where r_{ki} is the distance between particles i and k. The corresponding structure factor $S(q)$ is defined using the primary particle pair correlation function $g(r)$

$$S(q) = 1 + 4\pi N_p/V_p \int_0^\infty [g(r) - 1]\frac{\sin(qr)}{qr} r^2 dr \tag{13}$$

The behaviour of the structure factor of fractal agglomerates can be characterized by different regimes (Hyeon-Lee et al., 1998; Sorensen, 2001). For $qR_{G,Agg} \ll 1$, the structure factor approaches 1. For $qR_{G,Agg} < 1$, the structure factor results in the Guinier equation for the agglomerates. Its great utility is that it allows for measurement of the agglomerate size. For $R_{G,Agg}^{-1} < q < R_{G,P}^{-1}$, fractal agglomerates show a power-law scattering with a structure factor proportional to $(qR_{G,Agg})^{-D_f}$ and a fractal dimension D_f. For $q > R_{G,P}^{-1}$, the scattering curve holds information on the total surface in the scattering volume, which is described by Porods law $I(q) \sim q^{-4}$. The transition between the regimes is described mathematically by cut-off functions and can be adapted to experimental results by scattering simulations. Differences between various cut-off functions can often be distinguished only by numerical calculations. Thus, scattering curves of nanoscale agglomerates can be devided into three q ranges, which deliver the information on the primary particle and agglomerate sizes as well as the fractal dimension by fitting the experimental data, respectively.

Alternatively, a unified exponential and power-law approach proposed by Beaucage et al. allows analysis of the acquired SAXS curve for complex systems containing multiple levels of related structural features (Beaucage and Schaefer, 1994; Beaucage, 1995)

$$I(q) = \sum_{i=1}^{n}\left[G_i \cdot exp\left(\frac{-q^2 R_{G_i}^2}{3}\right) + B_i \cdot exp\left(\frac{-q^2 R_{G_{(i+1)}}^2}{3}\right) \cdot \left\{\frac{q}{\left[erf\left(\frac{qR_{G_i}}{\sqrt{6}}\right)\right]^3}\right\}^{-P_i}\right] \tag{14}$$

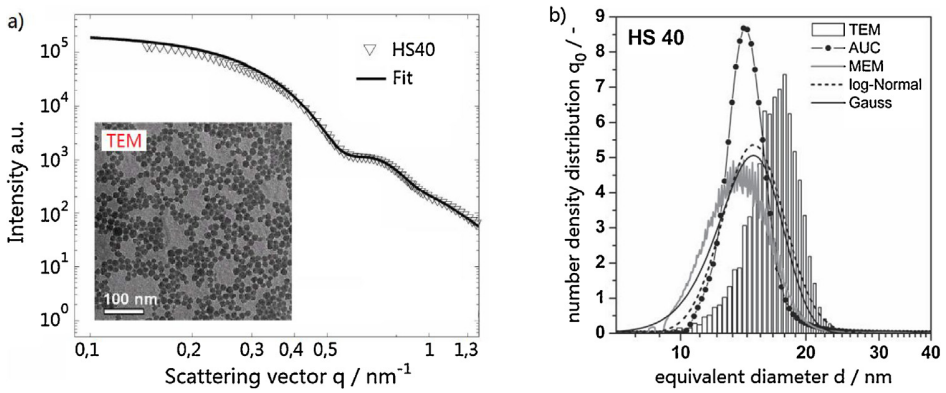

Fig. 3 – Comparison of the results for the number density distribution of silica particles HS40 measured by TEM, AUC and SAXS (Goertz et al., 2009b; Goertz, 2011). (a) TEM image and scattering curve; (b) Particle size distribution. Adapted from V. Goertz, N. Dingenouts and H. Nirschl, Part. Part. Syst. Charact. 26 (2009), 17–24, by permission of John Wiley and Sons.

where *erf* () is the error function, and i refers to the differently sized structures. For instance, the scattering intensity of two structural levels ($i = 2$) such as fractal agglomerates can be modelled as the combination of two Guinier fits and two power-law fits with Eq. (14). Thus, fitting the unified model to experimental data leads to the radii of gyration of the primary particles ($R_{G,P} = R_{G1}$) and agglomerates ($R_{G,Agg} = R_{G2}$), the mass fractal dimension of agglomerates ($D_m = D_f = P_2$), and the surface fractal dimenaion of particles ($D_s = 6 - P_1$) at large q. For ideal two-phase particle systems with sharp boundaries and smooth surface, D_s equals 2, which corresponds to Porod's law ($P_1 = 4$).

However, it is worth noting that for particles with rough surface the power-law exponent P_1 at large q is smaller than four ($3 < P_1 < 4$). When particles have a diffuse phase boundary, the electron density profile on the surface is not scharp but changes gradually between two phases. In this case, the measured parameter P_1 will deviate from Porod's law and have a value greater than four. Based on two electron density profile models, sigmoidal electron-density gradient model (Ruland, 1971) and linear electron-density gradient model (Vonk, 1973), the thickness E of the diffuse boundary nanostructured layer can be determined by processing the scattering data in the plot of $ln\left[I(q) \cdot q^4\right]$ *versus* q^2 at large values of scattering vector (Guo et al., 2013a)

$$ln[I(q) \cdot q^4] = \ln C_p - \sigma^2 q^2. \tag{15}$$

The slope of $-\sigma^2$ in Eq. (15) gives the value of the thickness $E = 2\sqrt{3}\sigma$.

Real particle systems are often polydisperse in size. The scattering intensity of a polydisperse system with a particle size distribution $D_N(r)$ is the contribution from each size fraction. Thus, Eq. (11) can be further written as

$$I(q) = \frac{N}{V} \Delta\rho_e^2 \int_0^\infty D_N(r) V_p^2(r) P(q,r) S(q,r) dr \tag{16}$$

The scattering pattern of a monodisperse suspension is characterized by maxima and minima resulting from the *sinc*-function in Eq. (4). The shape of each maximum is defined by the characteristic function $\gamma_0(r)$. The structure in the scattering pattern becomes less pronounced with increasing polydispersity, while the mean particle size determined from the scattering curve does not change. In practice, different particle size distribution functions are used to fit the experimental SAXS curves of nanostructured and functionalised particle systems such polydisperse spheres and core–shell nanocomposites (Dingenouts et al., 1994; Goertz et al., 2009b; Gutsche et al., 2014).

The wide-angle X-ray scattering signals simualteneously acquired with the SAXS–WAXS laboratory setup, as shown in Fig. 2, allow characterisation of crystalline structures of particles, such as identification of crystal phases, determination of crystal sizes and study on crystal phase transformation in the synthesis and/or after-treatment. The relationship between the mean crystal size D and the width of X-ray diffraction peak at wide angles can be described with the Scherrer equation (Klug and Alexander, 1974)

$$D = \frac{K \cdot \lambda}{FWHM \cdot \cos\theta} \tag{17}$$

where K is the Scherrer constant (0.9), θ is half of the scattering angle and $FWHM$ is the full width at half maximum of the X-ray diffraction peak.

4. Results and discussion

Some commercial nanoparticles have been firstly used as test samples to validate the SAXS results, which have been compared with those obtained with other measurement techniques. Fig. 3 exemplarily shows the experimental results for commercial silica dispersion Ludox HS40 (Grace Davision, Worms, Germany) studied by TEM, AUC and a SAXS camera equipped with a PSD gas-filled detector (Goertz et al., 2009b; Goertz, 2011). From the TEM micrograph (inset in Fig. 3a), it is seen that those silica particles are spherical and have a norrow size distribution. Further imaging analysis of the TEM micrograph leads to the particle size distribution (PSD) (histogram in Fig. 3b). As mentioned above, the scattering curve of a monodisperse suspension shows a typical structure characterized by maxima and minima. It is obvious that the acquired SAXS curve shows the oscillations with a somewhat less pronounced structure due to the polydispersity of the sample HS40 itself and can be well modelled with a Gaussian distribution function (solid line in Fig. 3a). Corresponding PSD by SAXS is displayed in Fig. 3b (solid line). Besides, the sample was also characterized by analytical ultracentrifuge *via* the measurement of the sedimentation behaviour and the resulting PSD is depicted with solid-dotted line in Fig. 3b. The mean

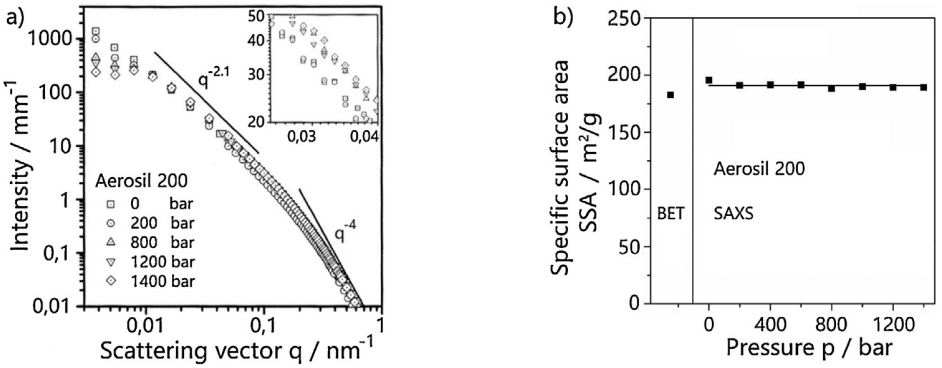

Fig. 4 – SAXS results of Aerosil 200 suspensions (Wengeler, 2007; Wengeler et al., 2007) (Reprinted (adapted) with permission from Characterizing Dispersion and Fragmentation of Fractal, Pyrogenic Silica Nanoagglomerates by Small-Angle X-ray Scattering, R. Wengeler, F. Wolf, N. Dingenouts and H. Nirschl, Langmuir, 2007, 23 (8), 4148–4154. Copyright 2007 American Chemical Society). (a) Scattering curves showing the influence of high pressure dispersion on Aerosil 200 suspension with a concentration of 0.1%. The inset shows a close up of scattering in the power law regime; (b) Specific surface area (SSA) for silica agglomerates from nitrogen adsorption (BET), as compared to SAXS measurements after high pressure dispersion at different pressure drops.

diameters by SAXS and AUC agree very well, while the mean diameter by TEM is somewhat bigger. This slight deviation is probably due to the poor contrast of particles and background in the TEM micrographs. In addition, manual image analysis of the chord length of every particle may also potentially lead to some errors. Nevertheless, the mean diameters measured with three different methods are very comparable. None of the distributions determined by TEM, SAXS or AUC is asymmetrical in terms of the mean diameter. In the whole, SAXS result is in good agreement with those by other measurement techniques. Furthermore, besides modelling of the scattering curve with a Gaussian distribution function, the PSD can also be retrieved with other methods such as log-normal model and maximum entropy method (Goertz et al., 2009b), as shown in Fig. 3b. Those results show that if a fixed distribution is used for the calculation of the scattering curve, a small scattering vector range around the first maxima is sufficient to determine the distribution parameters. In this scattering vector range the background noise is low and also minor interactions do not influence the results. In case that the size distribution is getting broader, the structure of the scattering curve gets less distinctive and the error of the results is increasing. Thus, the acquired SAXS curve can be further analysed with Guinier law, power law and/or so-called unified fit model to retrieve the structural parameters of the invesitaged samples.

In many particle handling processes, the knowledge of particle sizes and structures plays an important role in design, further optimization and utilization of the nanostructured particulate materials. For instance, high pressure dispersion of nanoscale particles and agglomerates can reduce the degree of agglomerates to generate small agglomerates or even primary particles in suspensions, which thus affects the material performance. To better understand the dispersion process and quantitatively characterize structural parameters, commercially available pyrogenic silica powder (Aerosil 200, Evonik, Germany) has been used and dispersed by high pressure ranging from 200 to 1400 bar, and the resulting suspensions were then investigated by USAXS (Wengeler, 2007; Wengeler et al., 2007). Due to the large agglomerate structures, the use of a synchrotron beamline (*e.g.* beamline ID02 ESRF, Grenoble, France) enables the accessibility of a smaller scattering vector q and thus a larger structure (Narayanan et al., 2001). Fig. 4a shows typical scattering curves for the resulting suspensions at different pressure drops. It is seen that high pressure dispersion process only has an impact on the low q-range, representing the Guinier regime of the agglomerates. Suspensions before dispersion and at low pressure drop of 200 bar show no pronounced Guinier regime where larger structures are still present. At higher pressure drops the slope at low q descreases, showing the reduced size of maximum agglomerates. Thus a Guinier fit can be applied to determine the radius of gyration $R_{G,Agg}$. The inset shows a close up of the power law regime. The order of the scattering intensities is inversed here compared to the Guinier regime. That is, high intensites in the Guinier region are lowest in the corresponding power law region, while low intensities for dispersed agglomerates are highest. In the power law regime, all curves have the same slope ($I \sim q^{-2.1}$) and thus they have the same mass fractal dimension $D_m = 2.1$. In the Porod regime ($I \sim q^{-4}$), the curves join into a single line which means that the primary particles are not affected and the Porod constant is unchanged. The rest of the curve is insensitive to dispersion. The corresponding parameters such as mass fractal dimension, primary particle size and the polydispersity are unchanged.

According to Eq. (8), SAXS allows to measure the specific surface area (SSA) of nanoparticles or agglomerates as dry powder or in a liquid suspension. Fig. 4b shows the specific surface areas of Aerosil 200 samples determined by SAXS and nitrogen adsorption (BET) method. The Aerosil 200 suspensions subjected to high pressure dispersion at different pressure drops show a nearly constant specific surface area, as indicated with a solid line in Fig. 4b. An agreement between BET and SAXS shows that no internal surface is present which would contribute to SAXS but is not accessible to nitrogen adsorption. The BET measurement for the suspension without any pressure fragmentation shows a slight reduction in SSA, which might be due to a closed structure inside the agglomerates and therefore just visible by SAXS. With high pressure dispersion no additional surface is produced by desagglomeration. The resulting SSA shows no trend and scatters around initial SSA with a standard deviation in the range of initial measurements. Hence, the sintered necks which are broken do not contribute significantly to the surface area. High pressure dispersion is characterized as a pure desagglomeration process where comminution, considered as a process of sur-

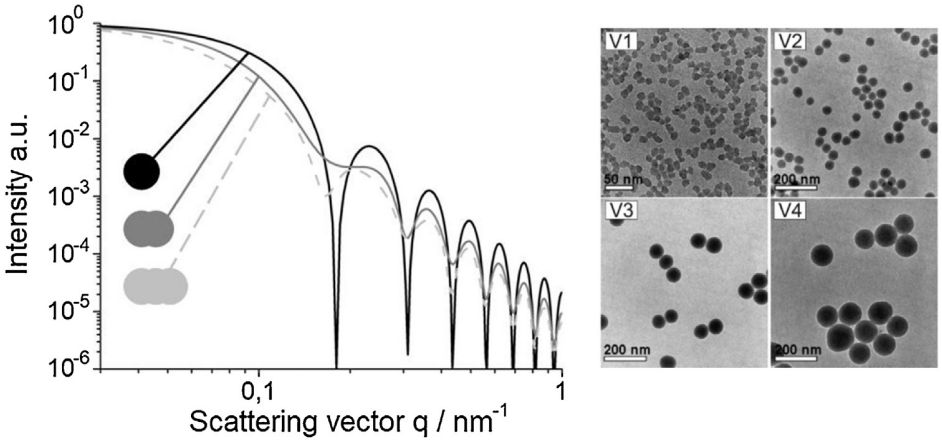

Fig. 5 – Comparison of the theoretical scattering curve of a sphere with the simulated scattering curve of a doublet and a triplet (left), and TEM images (right) of multiplets which can be generated by the Stöber reaction (Goertz, 2011; Goertz et al., 2012).
Reprinted (adapted) with permission from Small-Angle X-ray Scattering Study of the Formation of Colloidal SiO_2 Stöber Multiplets, V. Goertz, A. Gutsche, N. Dingenouts and H. Nirschl, J. Phys. Chem. C, 2012, 116 (51), 26938–26946. Copyright 2012 American Chemical Society.

face production due to the destruction of primary particles, is negligible (Wengeler, 2007; Wengeler et al., 2007).

Furtheron for the evaluation of experimental data of particle systems with respect to the aggregate structure and polydispersity, scattering curves can be simulated for aggregates composed of given numbers of primary particles, sometimes just two or three spheres (Goertz, 2011; Goertz et al., 2012). Because of the required spatial averaging, calculation of scattering intensity is more challenging than for radial symmetric systems. The scattering amplitude of radial symmetric systems can be calculated by a sinusoidal Fourier transformation of radial electron density distribution. However, for the mentioned non-symmetric multiplets, numerical methods have to be applied. For this purpose, a finite element method was applied to describe every particle structure in an approximate manner (Fedorov et al., 1974). The so-called sphere method was applied (Glatter, 1980). For the special case of a spherical particle, the form factor can calculated with Eq. (10). The scattering intensity of an aggregate of spheres is calculated then analytically according to Eq. (12). The first step of the simulation consists of generating multiplet structures. Subsequently, the object generation is followed by the calculation of scattering intensity.

For a SAXS analysis of multiplet structures, the scattering curves of a doublet and a triplet were simulated and compared with the theoretical scattering curve of a sphere at identical volume concentration (Fig. 5, left). The radii of the primary particles and the distances between the centres of mass have been fixed for the described configuration. The scattering curve of the sphere possesses the most pronounced structure. The larger the multiplet is, the steeper the decline of the scattering curve at small scattering vectors is. Compared to the scattering curve of the sphere, the intensity minimum and the first intensity maximum of the multiplets are shifted significantly towards smaller scattering vectors. Fig. 5 (right) shows TEM images of particles obtained from different synthesis routes V1 to V4 with classical Stöber method (Stöber et al., 1968). With a severe control of the mass flow of the precursor TEOS and the catalyst ammonia it was possible to design different multisphere structures. It can be concluded from the experiments V1 to V4 that a generation of multiplet structures by the Stöber process is possible. Size could be adapted

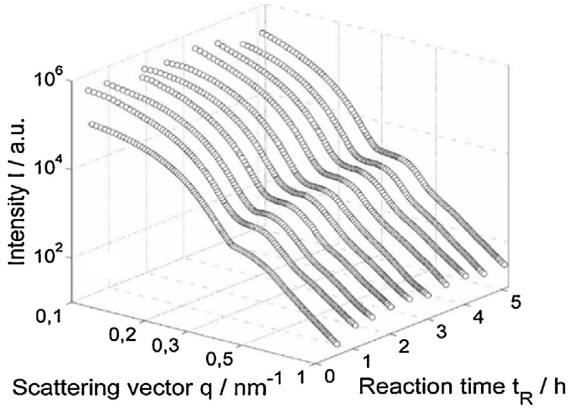

Fig. 6 – Scattering curve dependance on reaction time during multiplet formation (Goertz et al., 2012).
Reprinted (adapted) with permission from Small-Angle X-ray Scattering Study of the Formation of Colloidal SiO_2 Stöber Multiplets, V. Goertz, A. Gutsche, N. Dingenouts and H. Nirschl, J. Phys. Chem. C, 2012, 116 (51), 26938–26946. Copyright 2012 American Chemical Society.

by varying the precursor concentration and reaction temperature, with a higher precursor concentration and/or a smaller reaction temperature leading to a larger end particle size. With descreasing reaction temperature, hydrolysis reaction slows down and fewer nuclei were formed. By the adjustment of the particle-particle interaction (concentration, zeta potential, ion concentration) the multiplet formation could be controlled (Goertz et al., 2012).

Fig. 6 shows the scattering curves during the reaction of the multiplet formation process. At the beginning a distinguishable minimum can be observed which is typical for the spherical primary particles. With increasing reaction time and progressing growth of particles, the first intensity maximum and minimum are shifted towards smaller scattering vectors. This measurement represents the existence and development of multiplet structures. By an adjustment of the measured scattering curve with the described simulation, the multiplet structure, consisting of a specified number of particles or mixtures of multiplets, can be determined. As a restriction

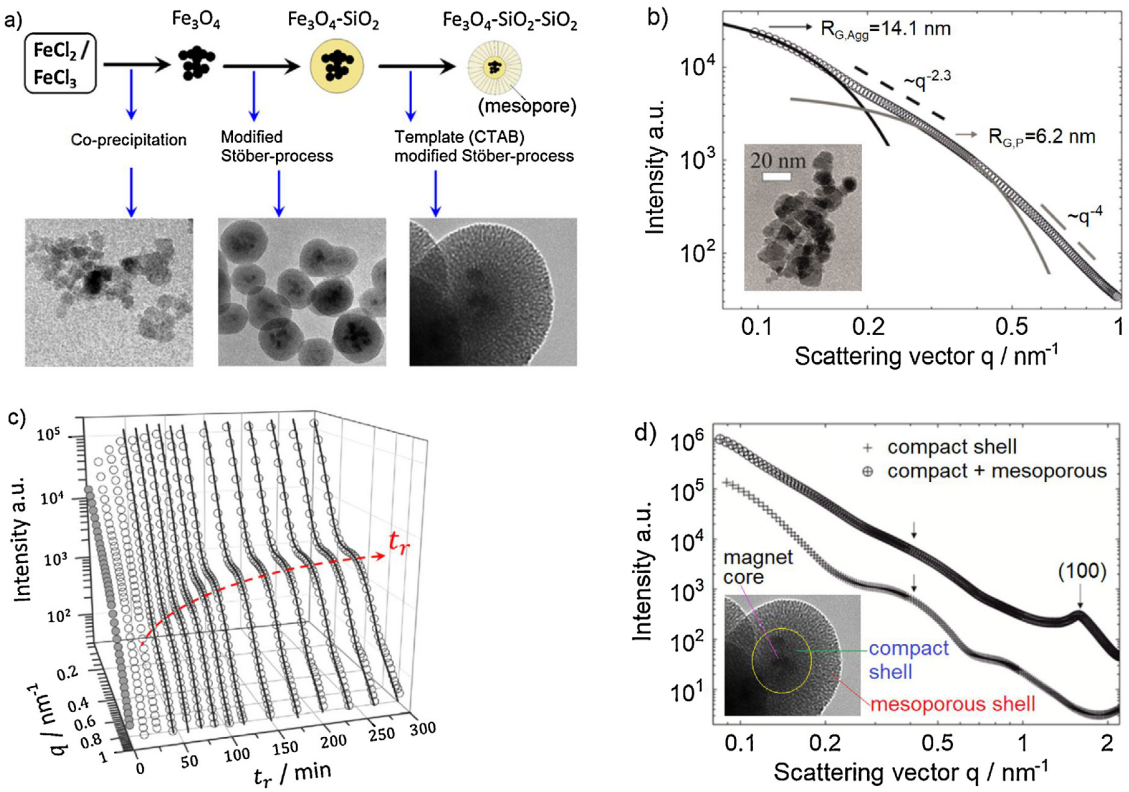

Fig. 7 – Time-resolved SAXS characterisation of the shell growth of silica-coated magnetite nanocomposites which were synthesized with co-precipitation followed by modified Stöber-process (Stöber et al., 1968; Gutsche et al., 2014) (Reprinted/Adapted by permission from Springer Nature: J. Nanopart Res (2014) 16: 2475 (Time-resolved SAXS characterization of the shell growth of silica-coated magnetite nanocomposites, A. Gutsche, A. Deikeler, X. Guo, N. Dingenouts and H. Nirschl), Copyright 2014). (a) Sketch of synthesis of magnetite nanoparticles and silica-coated nanocomposites with compact shell as well as compact and mesoporous shell structures; (b) Scattering curve of magnetite nanoparticles; (c) Scattering curves of core–shell magnetite particles changing with reaction time t_r and solid lines standing for the fitting curves by the core–shell sphere model; (d) Scattering curves of core–shell magnetite nanocomposites with compact shell and mesoporous shell structures.

it should be mentioned that primary particles are frequently polydisperse. This results in a smearing of the scattering data. Therefore, it is necessary to identifiy to which extent the scattering curve is affected and whether it is still possible to make a statement with respect to the aggregate structures. In general, it can be stated that the scattering curves of spheres have a much more pronounced structure than the doublet scattering curves at all distribution widths. The degree of smearing increases with increasing distribution width (Goertz et al., 2012).

Besides the above-discussed multiplet structures of silica particles, modified Stöber-process can also be used to synthesize other nanostructured particle systems, such as silica-coated magnetite nanocomposites. Such core–shell magnetite particles have advantages of high dispersibility and chemical stability, as compared to the conventional magnetic nanoparticles like Fe_3O_4 nanoparticles. The properties of the core–shell magnetite nanoparticles are strongly influenced by the shell thickness. Therefore, time-resolved *in-situ* monitoring of the shell thickness helps to know the shell growth kinetics, control the coating process and thus improve the product quality. To this end, a laboratory SAXS camera (Fig. 2c) has been used for time-resolved characterisation of shell growth during the synthesis. As shown in Fig. 7a, at first Fe_3O_4 nanoparticles were synthesized with the co-precipitation of $FeCl_3$ and $FeCl_2$ in alkaline media. The resulting black precipitate was separated, washed and stablized. The obtained Fe_3O_4 nanoparticles were later used as magnetite cores for further coating with silica using the modified Stöber-process (Stöber et al., 1968; Gutsche et al., 2014). The resulting compact silica-coated magnetite nanoparticles can be used as a basis to coat a second shell, *e.g.* a mesoporous shell structure formed using a template like cetyltrimethylammonium bromide (CTAB) or other shell structures. Details on the synthses can be found in (Gutsche et al., 2014). Here we focus on the structural characterisation of such different nanostructured particles by means of SAXS.

Fig. 7b depicts the scatterring curve of magnetite nanoparticles. It exhibits two-level structures without specific side maxima, indicating high polydispersity of magnetite particles. With Guinier law, the determined radius of gyration for primary particle $R_{G,P}$ is 6.2 nm. The power-law fit at large q follows Porod's law, i.e. $I \sim q^{-4}$, implying that the magnetite nanoparticles have smooth surfaces ($D_s = 2$). This agrees well with the TEM observation. Furthermore, in the small q range the scattering curve can be fitted with Guinier law and power law, leading to the radius of gyration for agglomerates ($R_{G,Agg} = 14.1$ nm) and the mass fractal dimension ($D_m = 2.3$), respectively. In the coating process, the dynamics of shell growth was monitored by time-resolved SAXS measurements. For instance, Fig. 7c illustrates the scattering curves of core–shell magnetite particles changing with reaction time

t_r. Solid lines stand for the fitting curves by the core–shell sphere model (Dingenouts et al., 1994; Gutsche et al., 2014). Before the coating reaction started, the SAXS curve at $t_r = 0$ looked very similar to that in Fig. 7b and did not exhibit any specific side maxima. After adding a defined amount of precursor TEOS to the prepared mixture (ammonia, ethanol, water and Fe_3O_4 solution), the coating process started and a silica shell grew on the Fe_3O_4 particle surface gradually by heterogeneous nucleation. Similar to kinetics of particle growth observed in Fig. 6, the progressing growth of shell thickness is visible in the SAXS curves after 30 min, indicated by a side maximum. With increasing reaction time, the silica shell becomes thicker and the side maximum is shifted to smaller scattering vector gradually, suggesting that the particles grow gradually with the time. It is also found that the measured SAXS curves can be well described with a core–shell sphere model and thus the shell thickness be can determined as a function of reaction time. Such time dependence of the shell thickness can be described by diffusion-limited growth kinetics of first order in precursor concentration (Sugimoto, 1987; Gutsche et al., 2014). The final shell thickness depends on the TEOS concentration. The SAXS results are in good agreement with TEM observation. Further experiments indicate that the final shell thickness can be controlled by adjusting the appropriate precursor concentration and reaction temperature. The synthesized silica-magnetite core–shell particles can be further coated. For instance, Fig. 7d shows the scattering curves of core–shell magnetite nanocomposites with compact shell and mesoporous shell structures, respectively. From the TEM micrograph in the inset of Fig. 7d, we can roughly distinguish three structures: magnetite core inside, mesoporous shell outside and compact shell in between. The characteristic "shoulder" shape for core–shell structures is visible in both scattering curves. In addition, a peak (100) occurs at $q_{peak} = 1.75\,\mathrm{nm}^{-1}$ in the SAXS curve of core–shell magnetite nanocomposites with mesoporous shell structures. This peak results from the diffraction effect due to the ordered porous structures formed by the used template. The mean distance between two pore centres can be estimated by $2\pi/q_{peak} \approx 3.6\,\mathrm{nm}$. Therefore, the laboratory SAXS camera allows for time-resolved study on the shell- and/or particle-growth kinetics and quantitative determination of structural parameters.

For dynamic *in-situ* characterization in particle synthesis processes operating in a continuous-flow mode, generally the reactor is connected to the SAXS setup with a tubing and the mixed reactants continuously flow through the sample cell. The reaction time, *i.e.*, the delay time between the reactor and the sample cell can be adjusted by varying the length and diameter of the tube as well as the flow rate. This allows direct online observation of the particle formation mechanisms. It should be mentioned that although there are numerous studies on *in-situ* X-ray scattering characterization of particle systems in various synthesis processes using synchrotron beamlines (Beaucage et al., 2004; Allen et al., 2008; St. John et al., 2013; Wu et al., 2018), to the best of our knowledge, still only very few reports deal with the time-resolved *in-situ* characterization of the early nucleation and growth kinetics with a laboratory SAXS instrument (Kehres et al., 2010; Polte et al., 2010; Chen et al., 2015). The modular-designed laboratory SAXS setups (Fig. 2) offer the possibility of *in-situ* characterization of nanostructured particles by adapting properly the reactor to the camera. For example, Goertz et al. used the laboratory SAXS camera for *in-situ* measurement of SiO_2 nanoparticles synthesized in a microwave-plasma reactor (Goertz et al., 2009a). Inside the plasma a gas mixture including TEOS vapour, oxygen, argon, and nitrogen was decomposed within a few microseconds followed by the formation of SiO_2 nanoparticles. The reaction chamber was integrated into the camera measurement section between collimation system and detector. The *in-situ* SAXS results were compared with online particle mass spectrometry and TEM measurements, showing a good agreement. Moreover, the lab-based SAXS camera was utilized for time-resolved *in-situ* characterization of aluminium-doped zinc oxide (AZO) nanocrystals in the non-aqueous sol–gel synthesis (Ungerer et al., 2018). The samples extracted from a batch reactor continuously flowed into a glass capillary inside the SAXS measurement chamber. This allowed time-resolved study of AZO nanoparticle formation and growth mechanisms, depending on synthesis parameters. In the continuous liquid-phase synthesis of nanostructured particles with defined properties like particle size distribution and morphology, for instance, a laminar flow reactor can be directly connected to the SAXS setup. Meier et al have recently used this *in-situ* setup to gain a better knowledge of the relevant mechanisms of SiO_2 nanoparticles *via* a modified Stöber process (Meier et al., 2018), which helped to know how to achieve compact and microporous SiO_2 nanoparticles by properly mixing the reactants and controlling the reaction temperature.

Besides the nanostructured particles produced in liquid-phase synthesis such as sol–gel method, in the past decades metallic nanoparticles synthesized in gas phase have been attacting more attention because of their unique size-dependent physicochemical properties and thus a vast number of applications. For example, electrical (spark, glow or arc) discharge synthesis in gases at atmospheric pressure has recently been further developed and optimized for better upscaling of production of nanoparticles and nanostructured materials in the recent EU-Project (BUONAPART-E: http://www.buonapart-e.eu/). Various measurement techniques have been further developed for product quality control and monitoring. Among them, a modified laboratory SAXS–WAXS measuring system allows very quick or quasi-online study of nanostructured materials synthesized in the gas phase at atmospheric pressure (Guo et al., 2013a,b, 2015a,b).

Fig. 8 exemplarily shows the SAXS–WAXS results of Cu nanoparticles synthesized by means of electrical discharge in the carrier gas of nitrogen (glow discharge, I = 0.5 A, gas flow rate Q = 10 l/min). The sample was obtained from the research group of Professor Einar Kruis at the University of Duisburg-Essen in Germany using an electrical discharge generator (Hontañón et al., 2013; Hontañón et al., 2014). Scattering intensity was measured by a laboratory SAXS–WAXS camera (Fig. 2d) with a wide detection angle 2θ up to 90° (Fig. 8a). The WAXS spectra allow identification of existent crystal phases. As compared to the background measurement (dashed line), some characteristic peaks (solid line) are visible in the scattering curve at wide angles. It is worth mentioning that in the background measurement the peaks visible in the WAXS curve (Fig. 8a and b) result from the sample holder and the low parasitical scattering of the measuring system itself. This effect can be removed by means of background substraction in the subsequent data analysis procedure. Further comparison with the XRD reference patterns (Lafuente et al., 2015) indicates that these characteristic peaks of the studied sample correspond to different crystal phases of Cu, CuO and

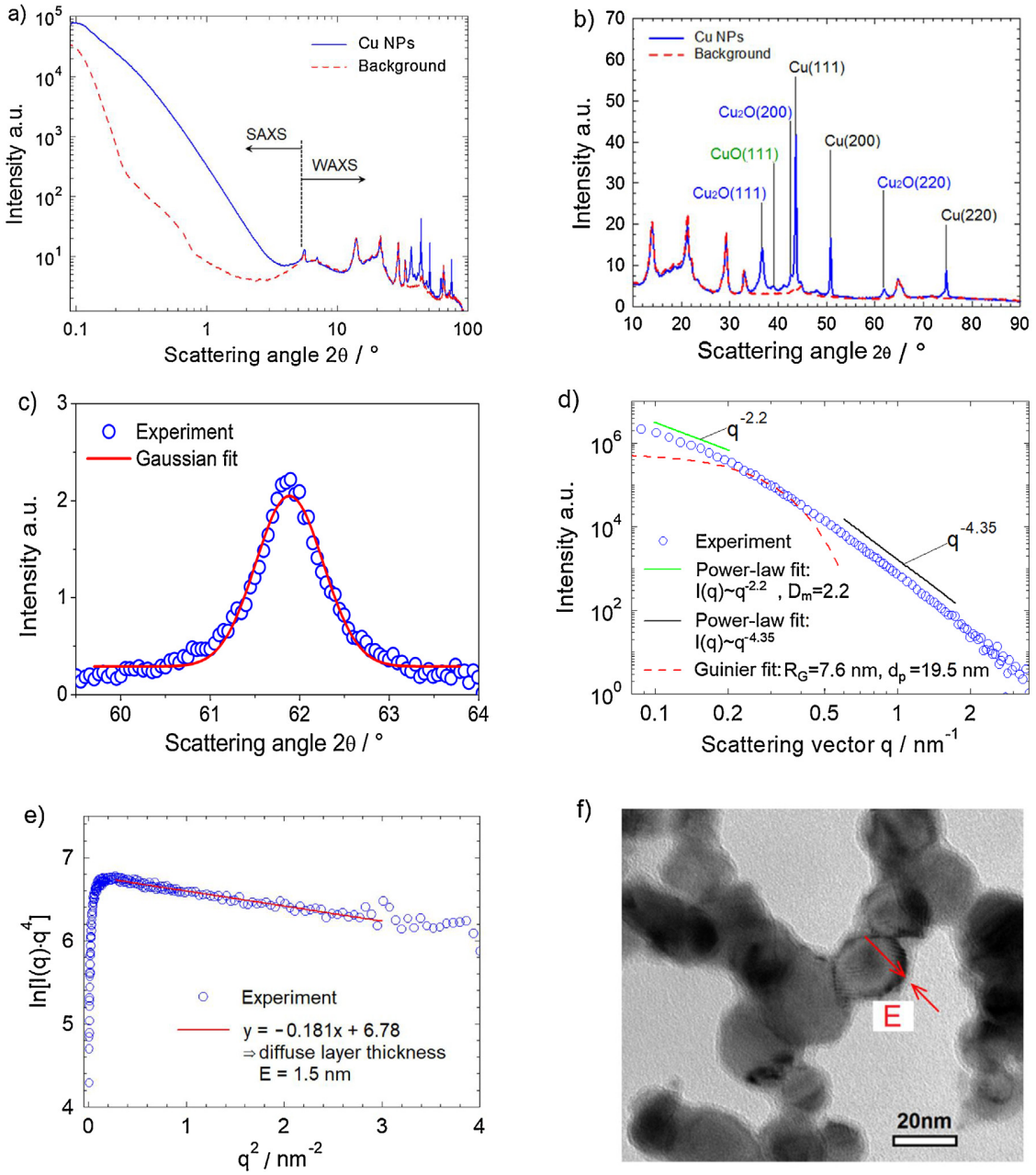

Fig. 8 – Results of Cu nanoparticles synthesized by means of electrical discharge in the carrier gas of nitrogen (glow discharge, I = 0.5 A, gas flow rate Q = 10 l/min). (a) Simultaneous SAXS–WAXS curves; (b) WAXS spectra; (c) Determination of mean crystal size of Cu_2O (220) peak with Gaussian fit of experimental data; (d) SAXS spectra; (e) ln $\left[I(q)\cdot q^4\right]$ *versus* q^2; (f) TEM micrograph.

Cu_2O, as indicated in Fig. 8b. Most contributions come from the pure Cu element inside nanoparticles; however, other visible peaks or crystal phases of CuO and Cu_2O may arise from the insufficient purity of the carrier gas or from the possible system leakage, leading to the formation of copper oxide. This helps to further optimize the synthesis process, *e.g.* by the use of higher purity carrier gas. On the other hand, a systematic oxidation of the particle surface can be used for passivation study. Meanwhile, this hints that it will be possible to generate metallic oxide nanoparticles by adjusting and controlling the carrier gas composition. The crystal phase size can be determined with Eq. (17). Fig. 8c depicts a crystal phase of Cu_2O (220). The experimental data were modelled with a Gaussian profile, leading to the peak position and the value of FWHM. Corresponding mean crystal size is *ca.* 10.3 nm. At small angles, the experimental SAXS curve was fitted in two power-law ranges and a Guiner range in between (Fig. 8d). The mass fractal dimension is 2.2 and the radius of gyration of primary particles is 7.6 nm, *i.e.* the mean particle diameter is 19.5 nm. The determined mean primary particle size agrees well with the TEM observation (Fig. 8f). It is interesting to find that the exponent of power-law fit at large q is greater than four ($I \sim q^{-4.35}$), implying that there exists a diffuse boundary nanostructure like thin oxide layer formed on the particle surface (Guo et al., 2013a,b). This diffuse boundary layer causes a gradual change of electron density and the thickness E is determined to be 1.5 nm with Eq. (15) in the plot of $ln\left[I(q)\cdot q^4\right]$ *versus* q^2, as shown in Fig. 8e. This also agrees well with the TEM observation (Fig. 8f).

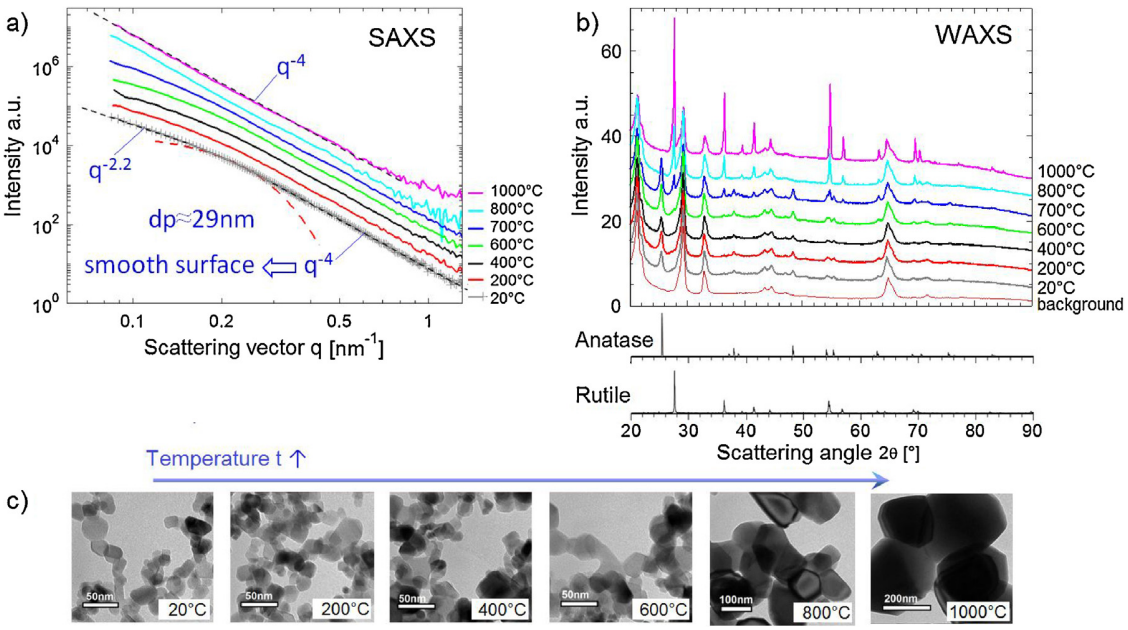

Fig. 9 – SAXS–WAXS results of TiO_2 nanoparticles in the calcination process under different conditions. Calcination temperature ranges from 200 up to 1000 °C. (a) SAXS spectra; (b) WAXS spectra; (c) TEM micrographs.

Above experimental results indicate that a wealth of quantitative information on the metallic nanostructured particles measured simultaneously by SAXS–WAXS enables further optimization of the gas-phase systhesis process and improvement of the product quality. Such SAXS–WAXS measuring system also allows investigation of other nanostructured materials, such as crystal phase transformation by calcination of crystalline nanoparticles at high temperature, and catalyst nanodots on the support particles produced by the combined chemical vapour synthesis (CVS) and chemical vapour deposition (CVD) (Heel and Kasper 2005; Binder et al., 2007; Guo et al., 2015a).

To study the crystal phase transformation of crystalline nanoparticles, a commercial sample titanium dioxide (AEROXIDE® TiO_2 P25, Evonik, Germany) was used and calcinated at different temperatures ranging from 200 up to 1000 °C. Before calcination, the original TiO_2 sample was also characterized at room temperature (20 °C). Corresponding SAXS–WAXS results are illustrated in Fig. 9. At room temperature, SAXS measurement shows a mass fractal dimension of 2.2 at small q and a mean primary particle size of 29 nm. The scattering intensity follows a power-law fit ($I \sim q^{-4}$) at large q in the SAXS curve (Fig. 9a), which suggests that the original sample has a smooth surface. With increasing calcination temperature, the "shoulder" of the SAXS curve is shifted to the small q range and the scattering intensity still obeys the Porod's law at large q. This suggests that the calcinated TiO_2 particles grow and become larger due to sintering at high temperature and that the calcination process has almost no effect on the particle surface roughness. That is to say, the surface fractal dimension remains constant ($D_s = 2$) and the samples have smooth surfaces. Such structural properties determined by SAXS are consistent with the TEM observation (Fig. 9c). As compared to the reference XRD database (Lafuente et al., 2015), original TiO_2 particles have both anatase and rutile phases identifiable in the acquired WAXS spectra (Fig. 9b). No significant difference between the WAXS curves is visible when the calcination temperature is lower than 600 °C. We can see more portion of rutile phase in the WAXS curve at 600 °C. This indicates that the anatase phase starts to transform into the rutile phase at *ca.* 600 °C. The diffraction patterns of rutile phase become predominant gradually and the diffraction peak height or intensity of rutile phase increases when the calcination temperature was increased from 600 to 1000 °C. These results clearly show that the phase transformation from anatase to rutile phase proceeds progressively with an increase in the temperature. It is found that when the temperature reaches 800 °C, the calcinated sample has only the rutile crystal structures, *i.e.* the anatase phase transforms into the rutile phase completely. Further increasing calcination temperature leads to a high crystallinity of the rutile phase and to an increase of crystal size, which is dominated by quite sharp and strong diffraction peaks of the rutile phase in the WAXS curve at 1000 °C (see top curve in Fig. 9b).

As regards the sintering effect on nanostructured particles at high temperature, another typical application example is the noble metal catalyst like Pt or Pd nanoparticles for automobile emission control and chemical production. Such metal catalyst nanodots, often deposited on oxide support particles, have larger active specific area and thus exhibit much higher catalytic activity than the bulk materials. Knowledge of the nanodot size and the morphology as well as the surface structure of the support particles helps to elucidate the metal-support interaction for stablization of nanodots, to control and adjust the surface roughness of support particles and thus to reduce the sintering at high temperature. For this purpose, support particles were produced by CVS and catalyst nanodots were deposited on the support particles by CVD (Heel and Kasper, 2005; Binder et al. 2007; Guo et al., 2015a). The prepared nanoparticles were characterized by SAXS–WAXS. For instance, Fig. 10 displays the SAXS–WAXS results of Pt nanodots (Pt-SiO_2) synthesized by the combined CVS and CVD process (Guo et al., 2015a). From the TEM micrograph, it is seen that the Pt nanodots were deposited on the SiO_2 support particles and formed small agglomerates (see inset in Fig. 10a). The mean primary particle size of Pt nanodots was determined to be 15.8 nm by analyzing the SAXS and image analysis of TEM micrographs led to a mean size of 13.8 nm. Both agree fairly

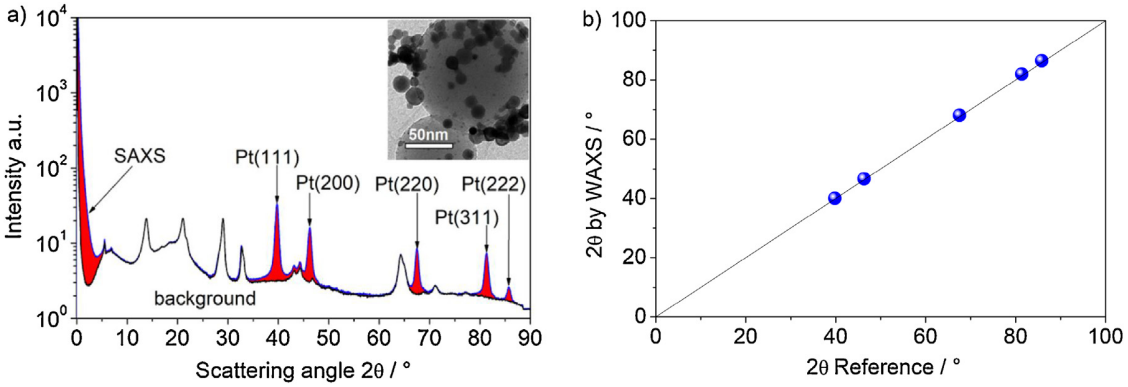

Fig. 10 – SAXS–WAXS results of Pt nanodots (Pt-SiO_2) synthesized by the combined CVS and CVD process (Guo et al., 2015a). (Reprinted/adapted from Powder Technology 272 (2015), X. Guo, K. Gao, A. Gutsche, M. Seipenbusch and H. Nirschl, Combined small- and wide-angle X-ray scattering studies on oxide-supported Pt nanoparticles prepared by a CVS and CVD process, pp23–33, Copyright (2015), with permission from Elsevier). (a) SAXS and WAXS spectra for determination of nanodot size and crystalline structure (Inset shows a TEM micrograph of Pt-SiO_2); (b) Comparison of Pt crystal phases measured by WAXS and reference data base.

Table 1 – Surface fractal dimensions D_s determined by SAXS for pure oxide support particles and their mixed-phase oxides with different mass fractions of Al_2O_3 (Guo et al., 2014).

Samples	Mass fraction of Al_2O_3 [–]	D_s [–]
Al_2O_3	1.00	2.15
SiO_2	0.00	2.04
TiO_2	0.00	2.01
SiO_2–Al_2O_3	0.06	2.21
	0.10	2.13
	0.45	2.12
TiO_2–Al_2O_3	0.40	2.06
	0.55	2.08
	0.58	2.10

well with each other. Five prominent diffraction peaks at wide angles correspond to the crystal phases of Pt (Fig. 10a). The positions 2θ of those five peaks correlate well with the reference data base (Fig. 10b). The mean crystal size determined with Eq. (17) is *ca.* 12 nm. This value obtained by WAXS is comparable to the mean primary particle sizes obtained by SAXS and TEM, implying that the primary Pt nanodots consist of single crystallites. Proper modification of the surface structures or roughness of support particles may help to stabilize metal catalyst nanodots against sintering and thus control the size of nanodots on the support particles. As proposed by Binder et al. (2010), introduction of a second oxide phase to the oxide support particles can modify the surface roughness of the formed oxide supports.

To further study the surface morphology of support particles, three different kinds of oxide support particles (SiO_2, TiO_2, Al_2O_3) and their binary mixed-phase oxides were synthesized in the gas phase by an integrated CVS and sintering process (Heel and Kasper, 2005; Binder et al. 2007; Guo et al. 2014). Their surface fractal dimensions D_s, which describe the roughness of particle surfaces, were quantitatively characterized by SAXS. Corresponding results are given in Table 1. It is seen that the surface fractal dimension of pure Al_2O_3 particles ($D_s = 2.15$) is larger than those of pure SiO_2 particles ($D_s = 2.04$) and pure TiO_2 particles ($D_s = 2.01$). This implies that the surface of pure Al_2O_3 particles is rougher than those of both pure SiO_2 and pure TiO_2 particles. By mixing a small amount of Al_2O_3 to SiO_2, the surface morphology of SiO_2 particles changes and the surface fractal dimension increases (*e.g.* $D_s = 2.21$ for a mass fraction of $Al_2O_3 = 0.06$), *i.e.* the particle surface becomes rougher. Further SAXS measurements indicate that a much larger fraction of Al_2O_3 in the SiO_2–Al_2O_3 mixed-phase oxides does not increase the surface roughness significantly. Similar surface morphological property was observed in the TiO_2–Al_2O_3 mixed-phase oxides. Rougher surface structure will help to prevent the deposited metal nanodots from migrating, colliding and sintering on the support particle surface and hence reduce the deactivation of supported metal catalysts. For this application, another potential alternative possibility is to produce SiO_2 nanoparticles with rough "gel-like" surface structures as support particles. Such SiO_2 particles covered with gel-like structured fine units can be prepared with modified Stöber process followed by evaporation of the solvent (Gutsche et al., 2015). TEM and SAXS analyses indicate that the gel-like surface structures formed by secondary nucleation consist of individual units of a few nanometers in size, almost independent of the reaction time at which the particle suspensions are sampled and heat-treated afterwards for evaporation of solvent. However, the amount of such surface structures changes with the reaction time, implying that the surface structure can be modified and controlled just by sampling and heating the Stöber-produced particle suspension at a proper reaction time. Above experimental results have shown that SAXS is a very powerful technique for non-invasive characterisation of numerous nanostructured materials.

5. Summary and conclusions

In this work we gave an overview about the SAXS measurement technology for non-invasive characterisation of nanostructured and functionalised particles. We demonstrated our laboratory SAXS camera system, which recently has been further developed and optimized for various applications based on the modular design. Through proper choice of a sample holder and/or measurement cell, the designed benchtop camera is suitable for quick *in-situ* measuring different disperse particulate systems, such as powders and suspensions as well as aerosol nanoparticles which can be deposited on a certain sample substrate. The detection angle of a new system reaches up to 90°, allowing simultaneous

SAXS and WAXS measurements. By extending the sample-to-detector distance, the available small scattering vector now enables structural analysis of particle systems on multiple scales ranging from about one nanometer to several hundred nanometers. In addition, the use of an on-line X-ray detector makes on-line *in-situ* analysis possible, too. Furthermore, different data processing methods and models have been introduced for analyzing the acquired scattering data and retrieving the structural parameters of the investigated particle systems.

Experimental results of some selected nanostructured and functionalised particles studied recently by SAXS–WAXS have shown that SAXS enables determination of primary particle size and size distribution, agglomerate size, surface and mass fractal dimensions describing the roughness of particle surface and the 3D mass-fractal network structures, specific surface area and the thickness of diffuse boundary nanostructured layer on the particle surface. Simultaneous WAXS spectra allow identification of crystal phases, determination of crystal sizes and investigation of crystal phase transformation. Particle size and size distribution by SAXS agree well with those by other techniques like TEM and analytical ultracentrifuge (AUC). In particle handling processes, SAXS results clearly indicated that high pressure dispersion process led to an obvious reduction of agglomerate size visible in the SAXS curves at small q, but almost no change of the primary particle size, the fractal dimension or specific surface area comparable to BET gas absorption measurement. For crystalline nanostructured particles like TiO_2, elevated calcination temperature from 200 °C up to 1000 °C led to the shift of the "shoulder" (Guinier range) in the SAXS curve to the small q range, implying an increase of primary particle size because of the sintering of particles. The surface fractal dimensions remain nearly constant ($D_s = 2$) throughout the calcination process, obeying the Porod's law and agreeing with the TEM observation. WAXS spectra revealed that the anatase phase of TiO_2 nanoparticles starts to transform into the rutile phase at *ca.* 600 °C and this phase transformation proceeds progressively with the temperature. When the temperature reaches 800 °C, the calcinated sample has only the rutile crystal structures, *i.e.* the anatase phase transforms into the rutile phase completely. In liquid-phase synthesis processes, SAXS enables investigation on the scattering from multiplet structures of silica particles and *in-situ* monitoring of growth kinetics of Stöber silica nanoparticles and core–shell magnetite nanocomposites. In gas-phase synthesis processes, metallic nanoparticles produced by electrical discharge in the carrier gas at atmospheric pressure were characterized by SAXS–WAXS and a wealth of structural information was simultaneous obtained. At wide angles different crystal phases were identified and corresponding mean crystal sizes were estimated with the Scherrer equation. Some unexpected crystal phases occuring in the WAXS curve, *e.g.* copper oxide crystal phases, revealed the oxidation due to the impurity of carrier gas or the possible system leakage, which did help to further optimize the synthesis process. Besides, the SAXS measurements gave the structural information on the primary particle size, the mass fractal dimension of the agglomerates and the thickness of the diffuse boundary nanostructured layer formed on the particle surface due to the oxidation. From the point of view of practical application, those SAXS–WAXS results give us a hint that proper adjustment of the carrier gas composition, *e.g.* presetting of the amount of oxygen in the carrier gas, allows synthesis of metallic oxide nanoparticles. Another typical application example in the gas-phase synthesis has shown that metal catalyst nanodots can be deposited on support particles by means of the CVS/CVD technique. Nanodot crystalline structures were obtained from the WAXS spectra, while the nanodot size and the surface structures of the support particles were quantitatively analysed by SAXS. Further SAXS study on the surface fractal dimensions of the oxide and mixed-phase oxide support particles suggests that the surface structure and roughness can be modified by introducing a second oxide phase to the oxide support particles. This is essential for stablization of the nanodots against sintering and improvement of the catalytic activity and efficiency.

Finally, it should be pointed out that for some special particulate systems with very low electron density contrast compared to their surrounding media, such as emulsions, liposoms, polymeric or organic particles, the scattering intensity from those samples will be very weak using a laboratory X-ray source and thus a very long measurement time will be needed. In the worst case, it is even not possible to characterize such particulate systems due to very bad signal-to-noise ratio by the use of a laboratory SAXS camera. In this case, utilization of highly brilliant synchrotron X-ray sources will be a preferable choice. However, considering the easy availability and unlimited design options, laboratory cameras have their own unique advantages and find many practical applications in the fields of material science, chemical reaction, process engineering, particle synthesis and aftertreatment, biomedicine and many others. On the other hand, the Bonse–Hart configuration enables laboratory pinhole SAXS cameras to probe ultrasmall-angle scattering signals which commonly occur in the range behind the beamstop in a conventional laboratory SAXS camera.

Acknowledgements

We gratefully acknowledge the funding from the European Union Seventh Framework Programme (FP7/2007–2013) under Grant Agreement No. 280765 (BUONAPART-E) and the financial support from the German Research Foundation (DFG Ni 414/13-1 and DFG Ni 414/22-1). We would like to thank Esther Hontañón and Professor Einar Kruis for kindly providing the metallic nanoparticles synthesized by electrical discharge, Kun Gao and Sven Richter for kindly providing the Pt-SiO_2 and oxide support particles by CVS/CVD, and Alexander Gutsche and Alexander Daikeler for preparing the magnetite core–shell nanoparticles.

References

Allen, A.J., Hackley, V.A., Jemian, P.R., Ilavsky, J., Raitano, J.M., Chan, S.W., 2008. In situ ultra-small-angle X-ray scattering study of the solution-mediated formation and growth of nanocrystalline ceria. J. Appl. Crystallogr. 41 (5), 918–929.

Beaucage, G., 1995. Approximations leading to a unified exponential/power-law approach to small-angle scattering. J. Appl. Crystallogr. 28 (6), 717–728.

Beaucage, G., Kammler, H.K., Mueller, R., Strobel, R., Agashe, N., Pratsinis, S.E., Narayanan, T., 2004. Probing the dynamics of nanoparticle growth in a flame using synchrotron radiation. Nature Materials 3, 370.

Beaucage, G., Schaefer, D.W., 1994. Structural studies of complex systems using small-angle scattering: a unified Guinier/power-law approach. J. Non Crys. Solids 172–174, 797–805.

Binder, A., Heel, A., Kasper, G., 2007. Deposition of palladium nanodots of controlled size and density onto surface-modified

SiO_2 particles by an atmospheric pressure CVS/MOCVD process. Chem. Vap. Depos. 13 (1), 48–54.
Binder, A., Seipenbusch, M., Kasper, G., 2010. Sintering of Pd catalyst particles on SiO_2-TiO_2 carrier particles of different mixing ratios. J. Phys. Chem. C 114 (17), 7816–7821.
Bonse, U., Hart, M., 1965. Tailless X-Ray single-crystal reflection curves obtained by multiple reflection. Appl. Phys. Lett. 7 (9), 238–240.
Chen, X., Schröder, J., Hauschild, S., Rosenfeldt, S., Dulle, M., Förster, S., 2015. Simultaneous SAXS/WAXS/UV–vis study of the nucleation and growth of nanoparticles: a test of classical nucleation theory. Langmuir 31 (42), 11678–11691.
Debye, P., 1915. Zerstreuung von Röntgenstrahlen. Annalen der Physik 351 (6), 809–823.
Dingenouts, N., Ballauff, M., 1998. Structural investigation of latexes by small-angle X-ray scattering in slitcollimation: measurements and evaluation of data. Acta Polymerica 49 (4), 178–183.
Dingenouts, N., Kim, Y.-S., Ballauff, M., 1994. Radial density distribution in core-shell latexes as revealed by small-angle X-ray scattering. Macromol. Rapid Commun. 15 (7), 613–617.
Dreiss, C.A., Jack, K.S., Parker, A.P., 2006. On the absolute calibration of bench-top small-angle X-ray scattering instruments: a comparison of different standard methods. J. Appl. Crystallogr. 39 (1), 32–38.
Fan, L., Degen, M., Bendle, S., Grupido, N., Ilavsky, J., 2010. The absolute calibration of a small-angle scattering instrument with a laboratory X-ray source. J. Phys.: Conf. Ser. 247 (1), 012005.
Fedorov, B.A., Ptitsyn, O.B., Voronin, L.A., 1974. X-ray diffuse scattering by proteins in solution. Consideration of solvent influence. J. Appl. Crystallogr. 7 (2), 181–186.
Feigin, L.A., Svergun, D.I., 2013. Structure Analysis by Small-Angle X-Ray and Neutron Scattering. Springer, US.
Fritz, G., Bergmann, A., 2006. SAXS instruments with slit collimation: investigation of resolution and flux. J. Appl. Crystallogr. 39 (1), 64–71.
Glatter, O., 1980. Computation of distance distribution-functions and scattering functions of models for small-angle scattering experiments. Acta Phys. Austr. 52, 243–256.
Glatter, O., Kratky, O., 1982. Small Angle X-ray Scattering. Academic Press Inc. Ltd., London.
Goertz, V., 2011. Untersuchungen zur Synthese und zum Wachstum von anorganischen Nanopartikeln in der Flüssig- und Gasphase mit Hilfe der Röntgenkleinwinkelstreuung. Dr. Hut.
Goertz, V., Abdali, A., Wiggers, H., Schulz, C., Nirschl, H., 2009a. In-situ small angle X-Ray scattering (SAXS) characterization of SiO_2 nanoparticles synthesized in a microwave-plasma reactor. In: European Aerosol Conference, Karlsruhe, Germany, Abstract T091A003.
Goertz, V., Dingenouts, N., Nirschl, H., 2009b. Comparison of nanometric particle size distributions as determined by SAXS, TEM and analytical ultracentrifuge. Part. Part. Syst. Charact. 26 (1–2), 17–24.
Goertz, V., Gutsche, A., Dingenouts, N., Nirschl, H., 2012. Small-angle X-ray scattering study of the formation of colloidal SiO_2 Stöber multiplets. J. Phys. Chem. C 116 (51), 26938–26946.
Guinier, A., Fournet, G., 1955. Small-angle Scattering of X-rays. John Wiley & Sons, Inc, New York.
Guo, X., Gao, K., Gutsche, A., Seipenbusch, M., Nirschl, H., 2014. Small-angle X-ray scattering study of surface morphology of oxide support particles synthesized by CVS and sintering. In: Conference on Aerosol Technology, Karlsruhe, Germany, Abstract T315A304.
Guo, X., Gao, K., Gutsche, A., Seipenbusch, M., Nirschl, H., 2015a. Combined small- and wide-angle X-ray scattering studies on oxide-supported Pt nanoparticles prepared by a CVS and CVD process. Powder Technol. 272, 23–33.
Guo, X., Gutsche, A., Nirschl, H., 2013a. SWAXS investigations on diffuse boundary nanostructures of metallic nanoparticles synthesized by electrical discharges. J. Nanopart. Res. 15 (11), 2058.
Guo, X., Gutsche, A., Wagner, M., Seipenbusch, M., Nirschl, H., 2013b. Simultaneous SWAXS study of metallic and oxide nanostructured particles. J. Nanopart. Res. 15 (4), 1559.
Guo, X., Wagner, M., Gutsche, A., Meyer, J., Seipenbusch, M., Nirschl, H., 2015b. Laboratory SWAXS combined with a low-pressure impactor for quasi-online analysis of nanoparticles generated by spark discharge. J. Aerosol Sci. 85, 17–29.
Gutsche, A., Daikeler, A., Guo, X., Dingenouts, N., Nirschl, H., 2014. Time-resolved SAXS characterization of the shell growth of silica-coated magnetite nanocomposites. J. Nanopart. Res. 16 (7), 2475.
Gutsche, A., Dingenouts, N., Guo, X., Meier, M., Nirschl, H., 2016. Probing the absolute scattering intensity by means of a laboratory-based small-angle X-ray scattering camera using an imaging plate detector. J. Appl. Crystallogr. 49 (1), 15–23.
Gutsche, A., Guo, X., Dingenouts, N., Nirschl, H., 2015. Synthesis and small angle X-ray scattering (SAXS) characterization of silica spheres covered with gel-like particles formed by means of solvent evaporation. Powder Technol. 278, 257–265.
Gutsche, A., Meier, M., Guo, X., Ungerer, J., Nirschl, H., 2017. Modification of a SAXS camera to study structures on multiple scales. J. Nanopart. Res. 19 (9), 321.
Heel, A., Kasper, G., 2005. Production and characterization of Pd/SiO_2 catalyst nanoparticles from a continuous MOCVS/MOCVD aerosol process at atmospheric pressure. Aerosol Sci. Technol. 39 (11), 1027–1037.
Hontañón, E., Palomares, J.M., Guo, X., Engeln, R., Nirschl, H., Kruis, F.E., 2014. Influence of the inter-electrode distance on the production of nanoparticles by means of atmospheric pressure inert gas dc glow discharge. J. Phys. D: Appl. Phys. 47 (41), 415201.
Hontañón, E., Palomares, J.M., Stein, M., Guo, X., Engeln, R., Nirschl, H., Kruis, F.E., 2013. The transition from spark to arc discharge and its implications with respect to nanoparticle production. J. Nanopart. Res. 15 (9), 1957.
Hyeon-Lee, J., Beaucage, G., Pratsinis, S.E., Vemury, S., 1998. Fractal analysis of flame-synthesized nanostructured silica and titania powders using small-angle x-ray scattering. Langmuir 14 (20), 5751–5756.
Kehres, J., Andreasen, J.W., Krebs, F.C., Molenbroek, A.M., Chorkendorff, I., Vegge, T., 2010. Combined in situ small and wide angle X-ray scattering studies of TiO_2 nano-particle annealing to 1023 K. J. Appl. Crystallogr. 43 (6), 1400–1408.
Klug, H.P., Alexander, L.E., 1974. X-Ray Diffraction Procedures: For Polycrystalline and Amorphous Materials. Wiley.
Kratky, O., 1954. Neues Verfahren zur Herstellung von blendenstreuungsfreien Röntgen-Kleinwinkelaufnahmen. Zeitschrift für Elektrochemie, Berichte der Bunsengesellschaft für physikalische Chemie 58 (1), 49–53.
Lafuente, B., Downs, R.T., Yang, H., Stone, N., 2015. The power of databases: the RRUFF project. In: Armbruster, T., Danisi, R.M. (Eds.), Highlights in Mineralogical Crystallography. De Gruyter, Berlin, pp. 1–30.
Meier, M., Ungerer, J., Nirschl, H., 2018. Continuous synthesis and in situ SAXS analysis of silica nanoparticles in liquid phase. In: 8th World Congress on Particle Technology, Orlando, USA.
Narayanan, T., Diat, O., Bösecke, P., 2001. SAXS and USAXS on the high brilliance beamline at the ESRF. Nucl. Instrum. Methods Phys. Res. A: Accel. Spectrom. Detect. Assoc. Equip. 467–468 (Part 2), 1005–1009.
Orthaber, D., Bergmann, A., Glatter, O., 2000. SAXS experiments on absolute scale with Kratky systems using water as a secondary standard. J. Appl. Crystallogr. 33 (2), 218–225.
Polte, J., Erler, R., Thünemann, A.F., Sokolov, S., Ahner, T.T., Rademann, K., Emmerling, F., Kraehnert, R., 2010. Nucleation and growth of gold nanoparticles studied via in situ small angle X-ray scattering at millisecond time resolution. ACS Nano 4 (2), 1076–1082.

Renaud, G., Lazzari, R., Leroy, F., 2009. Probing surface and interface morphology with grazing incidence small angle X-ray scattering. Surf. Sci. Rep. 64 (8), 255–380.
Ruland, W., 1971. Small-angle scattering of two-phase systems: determination and significance of systematic deviations from Porod's law. J. Appl. Crystallogr. 4 (1), 70–73.
Sakka, S., 2005. Handbook of Sol-gel Science and Technology. 2. Characterization and Properties of Sol-gel Materials and Products. Kluwer Academic Publishers.
Sorensen, C.M., 2001. Light scattering by fractal aggregates: a review. Aerosol Sci. Technol. 35 (2), 648–687.
St. John, S., Hu, N., Schaefer, D.W., Angelopoulos, A.P., 2013. Time-resolved, in situ, small- and wide-angle X-ray scattering to monitor pt nanoparticle structure evolution stabilized by adsorbed $SnCl_3$-ligands during synthesis. J. Phys. Chem. C 117 (15), 7924–7933.
Stöber, W., Fink, A., Bohn, E., 1968. Controlled growth of monodisperse silica spheres in the micron size range. J. Colloid Interface Sci. 26 (1), 62–69.
Sugimoto, T., 1987. Preparation of monodispersed colloidal particles. Adv. Colloid Interface Sci. 28 (Suppl. C), 65–108.
Ungerer, J., Meier, M., Nirschl, H., 2018. Time-resolved characterization of customized aluminum-doped zinc oxide nanocrystals by means of small-angle X-ray scattering. In: 8th World Congress on Particle Technology, Orlando, USA.
Vonk, C., 1973. Investigation of non-ideal two-phase polymer structures by small-angle X-ray scattering. J. Appl. Crystallogr. 6 (2), 81–86.
Wengeler, R., 2007. Hydrodynamic Stress Induced Dispersion of Nanoscale Agglomerates by a High Pressure Process. Cuvillier.
Wengeler, R., Wolf, F., Dingenouts, N., Nirschl, H., 2007. Characterizing dispersion and fragmentation of fractal, pyrogenic silica nanoagglomerates by small-angle X-ray scattering. Langmuir 23 (8), 4148–4154.
Wu, L., Fournier, A.P., Willis, J.J., Cargnello, M., Tassone, C.J., 2018. In situ X-ray scattering guides the synthesis of uniform PtSn nanocrystals. Nano Lett.
Zhang, F., Ilavsky, J., Long, G.G., Quintana, J.P.G., Allen, A.J., Jemian, P.R., 2010. Glassy Carbon as an absolute intensity calibration standard for small-angle scattering. Metall. Mater. Trans. A 41 (5), 1151–1158.